Stable large-area monodomain in as-grown bulk ferroelectric single crystal $Sn_2P_2S_6$*

Yingzhuo Lun[†], Jiaqian Kang[†], Wenfu Zhu[†], Jianming Deng[†,‡], Xingan Jiang[†], Cheng Zhu[§],
Qi Ren[†], Xian Zi[†], Ziyan Gao[†], Tianlong Xia[¶], Zishuo Yao[‖], Xueyun Wang[†,**,§§] and Jiawang Hong[†,††,§§]

[†]School of Aerospace Engineering, Beijing Institute of Technology, Beijing 100081, P. R. China

[‡]Guangdong Provincial Key Laboratory of Electronic Functional Materials and Devices
Huizhou University, Huizhou, Guangdong 516007, P. R. China

[§]Advanced Research Institute of Multidisciplinary Science
Beijing Institute of Technology, Beijing 100081, P. R. China

[¶]Beijing Key Laboratory of Optoelectronic Functional Materials & Micro-nano Devices
Department of Physics, Renmin University of China, Beijing 100872, P. R. China

[‖]School of Chemistry and Chemical Engineering, Beijing Institute of Technology
Beijing 100081, P. R. China

[**]xueyun@bit.edu.cn

[††]hongjw@bit.edu.cn

Driven by the minimization of total energy, the multi-domain morphology is preferred in as-grown ferroelectrics to reduce the depolarization and strain energy during the paraelectric to ferroelectric phase transition. However, the complicated multi-domain is not desirable for certain high-performance ferroelectric electro-optic devices. In this work, we achieve a reproducible and stable large-area monodomain in as-grown bulk ferroelectric single crystal $Sn_2P_2S_6$. The monodomain dominates the entire single crystal, which is attributed to the internal charge carriers from the photoexcited disproportionation reaction of Sn ions. The charge carriers effectively screen the depolarization field and therefore decrease the depolarization energy and facilitate the formation of monodomain. This work offers a potential approach for engineering bulk ferroelectrics with a stable monodomain, which is desirable for the high-performance ferroelectric electro-optic devices.

Keywords: $Sn_2P_2S_6$; monodomain; ferroelectricity; piezoelectric force microscopy; disproportionation reaction; charge carriers; depolarization field screening.

1. Introduction

Ferroelectric materials attract intensive attentions due to their uniquely reversible polarization switching property and high dielectric performance, thus having promising applications in the energy harvesters,[1] nonvolatile memory devices[2,3] and novel multi-fields coupling electronic devices.[4,5] For example, tin-hypothiodiphosphate ($Sn_2P_2S_6$) is a nonoxide ferroelectric semiconductor with monoclinic *Pn* structure at room temperature. The advanced optical characteristics of low optical gap near 2.3 eV and great electro-optical properties[6–8] make it a promising application in photorefractive and dynamic holography optical devices.[9,10]

The competition of multiple energies, including the electrostatic, depolarization, elastic strain, and domain wall energies, usually facilitates complicated multi-domains in ferroelectrics to minimize the total energy.[11–13] However, the complicated multi-domain is not desirable for the requirement of certain ferroelectric electro-optical devices.[14,15] For example, the scattering from the multi-domain walls or twin boundaries causes serious optical losses, which degrades the optical performances.[15] On the contrary, the monodomain is of great significance to improve the performance of devices but hard to realize, especially in as-grown ferroelectric single crystals. The characteristic domain size w in the multi-domain of as-grown ferroelectrics is directly proportional to the square root of the thickness t (i.e., the well-known Landau–Kittel's scaling law,[16–18] $w^2 \sim t$). This scaling law is the consequence of the competition between the depolarization energy and the domain wall energy and it has been proved to be valid in bulk ferroics oxides,[18,19] ferroics thin films[20–22] and even in van der Waal's ferroelectrics.[23] The approach to break through the limited domain size so as to achieve stable monodomain in ferroelectrics becomes a critical issue. The screening of depolarization field is demonstrated as an

effective way to form stable monodomain in previous works. For example, the monodomain can be realized in the epitaxial ferroelectric oxide films by inserting a conductive layer or exposing the film surfaces to vapor environment.[24–26] These approaches provide extrinsic free compensation charges to screen the depolarization field. In addition, the interfacial strain engineering provides a strategy for controlling the in-plane monodomain in the epitaxial ferroelectric oxide films.[27] However, the above-developed methods strongly rely on the substrates and are therefore difficult to implement in bulk ferroelectrics. The control of stable monodomain remains a key challenge in bulk ferroelectrics.

In this work, we achieve a stable large-area monodomain in as-grown bulk ferroelectric single crystal $Sn_2P_2S_6$ (SPS), utilizing the ferroelectric hysteresis loop measurements and piezoelectric force microscopy. The monodomain is dominant in entire SPS crystal, except that the limited multi-domain is mainly nucleated at the edges. The analysis suggests that the depolarization field screening effect caused by internal charge carriers from photoexcited disproportionation reaction of Sn ions is responsible for the stable monodomain in SPS crystals. The special multi-domain morphologies at two opposite edges further validate the above mechanism, underlying the formation of monodomain. This work offers a potential principle for designing stable monodomain in bulk ferroelectrics, promoting the development of high-performance ferroelectric electro-optic devices.

2. Materials and Methods

2.1. *Sample preparation and characterizations*

The single crystals of SPS were synthesized by chemical vapor transport (CVT) method and the light illumination was naturally introduced during the cooling process. Stoichiometric amounts of Sn, P and S were ground together and then transferred to an evacuated quartz tube (pressure was ~3 × 10^{-4} Pa). The quartz tube was placed in a two-zone furnace (650–600°C). The temperature sequence is as follows: The quartz tube was heated to 550°C and kept for 12 h and then slowly heated to 660°C using 30 h, then kept for 120 h before furnace cooling to room temperature. During the annealing of SPS crystals in dark, the aluminum foil was wrapped around the evacuated quartz tube to avoid the illumination as much as possible. The annealed temperature was set as 120°C which is higher than the Curie temperature T_c. The single-crystal X-ray diffraction (XRD) experiments were performed using a Rigaku Oxford XtaLAB PRO diffractometer with graphite-monochromatic Mo Kα radiation (λ = 0.71073 Å) at room temperature. The crystal surface of the SPS crystal was identified by XRD collected from a Bruker D8 Advance X-ray diffractometer using Cu Kα radiation. The energy dispersive spectrum (EDS) were performed using a commercial ultra-high resolution cold-field emission scanning electron microscopy system (Hitachi, Regulus 8230) to check the elemental compositions.

2.2. *Measurements of ferroelectric and electrical properties*

The ferroelectric domain of the samples was imaged using a commercial atomic force microscope (Asylum Research MFP-3D). Before the piezoresponse force microscope (PFM) measurements, the SPS crystals with perfect natural as-grown/cleavage surface were selected using the optical microscopy. Then, the sample was attached to the conductive plate using silver paste, which acts as the bottom electrode in PFM measurements. The surface topography of testing sample was imaged and the corresponding surface roughness was determined to be ~0.25 nm. The PFM measurements were conducted using a conductive Si cantilever with Ti/Ir-coated tip. The spring constant of cantilevers is ~2.0 N/m and the tip-sample contact force was set as ~50 nN. The out-of-plane (OP) phase and amplitude images were acquired using the dual-frequency resonance tracking piezoresponse force microscopy (DART-PFM) mode. The conductive Si cantilever was excited with an *ac* voltage of 0.8 V at the tip-sample contact resonant frequency of ~350 kHz. The scanning rate was set as 0.5 Hz to improve the quality of images. The switching spectroscopy PFM (SS-PFM) was performed in DART mode. The hysteresis loops of the OP phase and amplitude signals were acquired to characterize the local ferroelectricity. The macroscopic ferroelectric hysteresis loops and current density-electrical field (*J-E*) curves at room temperature were measured using a standard ferroelectric tester (Radiant Technology, Multiferroic II, USA).

3. Results and Discussion

The elemental composition of Sn : P : S = 19.7 : 21.6 : 58.7 is confirmed using the EDS, as shown in Fig. 1(a). The result is consistent with the stoichiometric composition of SPS single crystal. The corresponding element mappings show chemical homogeneity in the grown crystals. The top facet of the specimen is confirmed as (011) surface using the XRD measurement, as shown in Fig. 1(b). The crystal structures for the ferroelectric and paraelectric phases have been examined as monoclinic noncentrosymmetric *Pn* ($T < T_c$) and centrosymmetric $P2_1/n$ ($T > T_c$), where the Curie temperature T_c is 339 K in the previous work.[7] The ferroelectricity of SPS crystals at room temperature is confirmed by the polarization versus electrical field (*P-E*) hysteresis loops and the corresponding polarization current peaks curves, as shown in Figs. 1(c) and 1(d). The spontaneous polarization and coercive field are determined as ~1.9 μC/cm² and ~0.23 kV/cm respectively.

PFM measurements were carried out to investigate the ferroelectric domain in the as-grown SPS crystals. The optical image of SPS crystal #1 with flat surface is shown in Fig. 2(a). The corresponding PFM OP phase image in Fig. 2(b) shows two distinct domains in purple and yellow colors. The mono-domain in purple is dominant in the entire crystal, except for
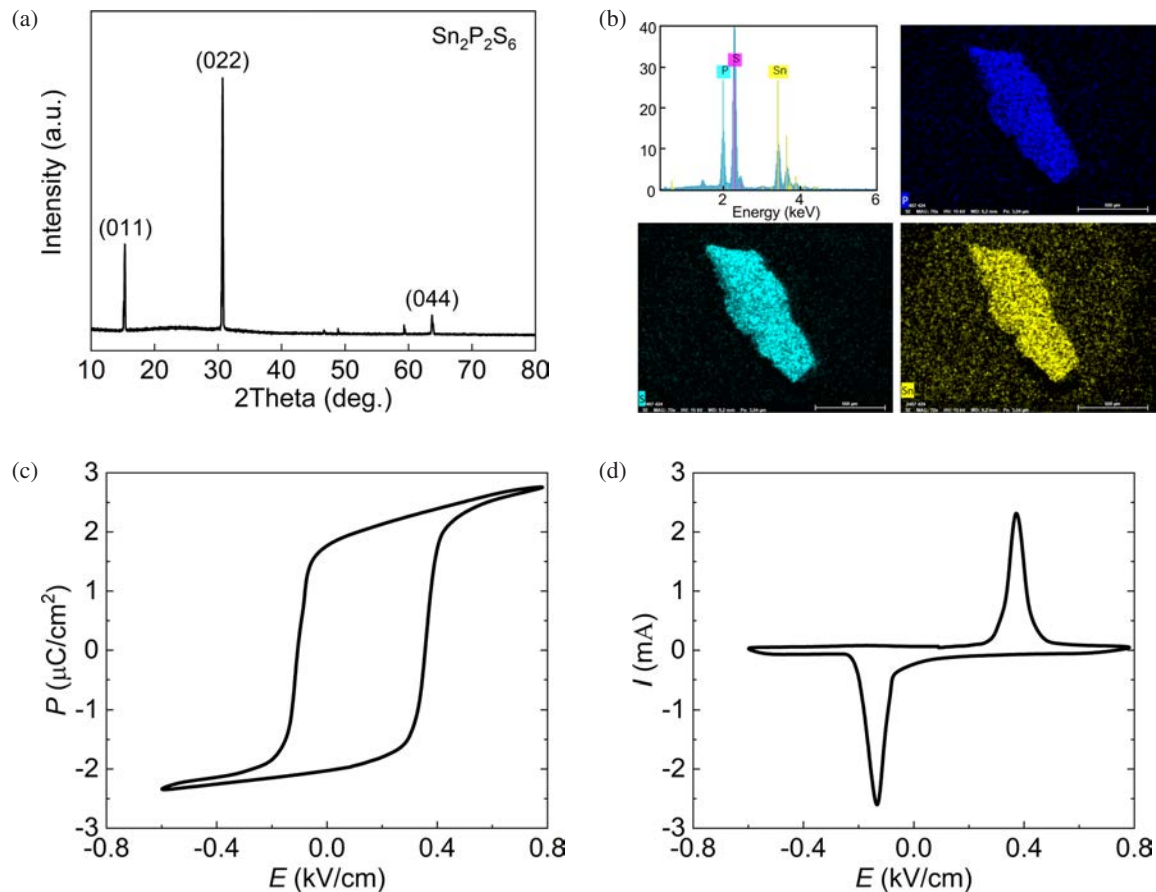
Fig. 1.   Characterizations of single crystal quality and ferroelectricity. (a) XRD pattern; (b) EDS and corresponding mappings for individual elements of Sn, S and P in single crystal $Sn_2P_2S_6$; (c) Polarizaition versus electrical field hysteresis loops and (d) corresponding polarization current versus electrical field curves at room temperature.

a limited multi-domain nucleated at the bottom edge (magnified in Fig. 2(c)). The characteristic size of fragmented random domains in the multi-domain region (Fig. 2(c)) is 1–8 μm and the farther from the bottom edge, the smaller the size. To verify that the large-area monodomain in purple was not an artifact of the PFM measurements, the local SS-PFM test was conducted in this region to characterize the reversible switching of ferroelectric polarization. As shown in Fig. 2(d), the local ferroelectricity is confirmed with the OP amplitude and phase versus bias voltage hysteresis loops, which show a piezoresponse well. The OP phase versus bias voltage hysteresis loop demonstrates that the local ferroelectric polarization can be switched with an applied electrical field of ~0.20 kV/cm by an AFM tip, which is consistent with the coercive field obtained from the macroscopic *P-E* measurements in Figs. 1(c) and 1(d).

The large-area monodomain is reproducible and stable in various as-grown SPS crystals. The PFM characterization results of another large-sized (~185 μm^2) SPS single crystal #2 are shown in Figs. 2(e) and 2(f). Similarly, the limited multi-domain is mainly nucleated at the right edge with large-area monodomain in the rest of the crystal. The width of the

multi-domain region is about 15 μm from the edge, similar to the SPS single crystal #1. In addition, there are two perpendicular cracks on the surface of SPS crystal #2, as marked in Fig. 2(e). A stripe domain in yellow with a width of ~3 μm is formed along the left side of the crack I, while the region at the right side of the crack I is persisted in monodomain, as shown in Fig. 2(f). However, another crack II perpendicular to the crack I exhibits a same domain in purple at the top and bottom sides of the crack. The PFM results of the local region marked with a white box around the crack I in Fig. 2(f) are magnified in Figs. 2(g) and 2(i). The 180° OP phase difference in two distinct regions (Fig. 2(g)) and the obviously weak OP piezoresponse at domain wall (Fig. 2(h)) indicates the anti-parallel orientation of spontaneous polarization in two different ferroelectric domains. The flat topography in Fig. 2(i) is confirmed to be independent with the different domains at two opposite sides of the crack I.

The formation mechanism underlying the large-area monodomain that dominates the entire samples in SPS crystal will be discussed in the following. Intuitively, the existence of an external conjugate electric field or flexoelectric field during the growth may cause preferential formation of
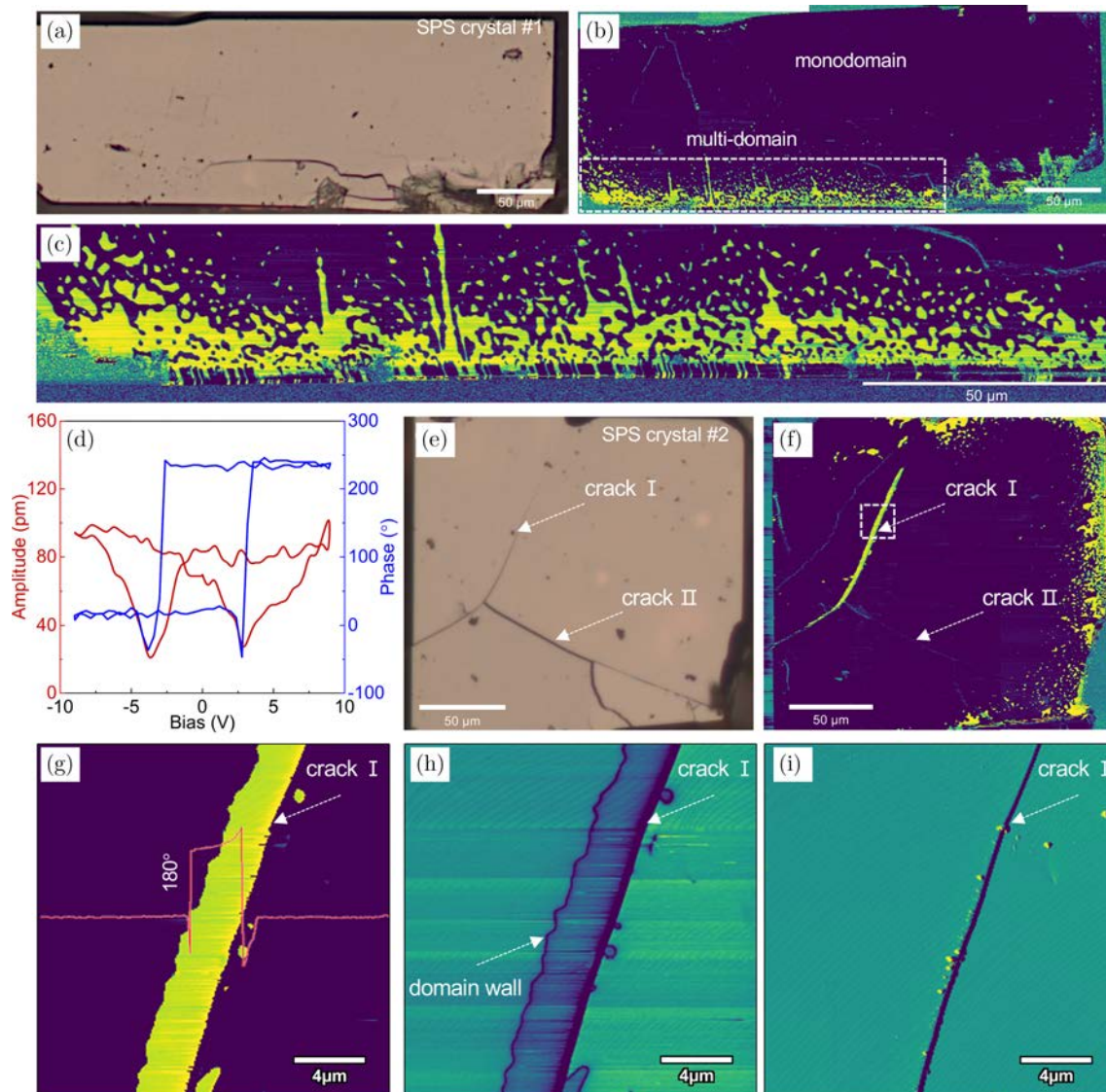
Fig. 2. Ferroelectric domain characterizations in SPS crystals. (a) Optical image and (b) corresponding OP phase image of SPS crystal #1; (c) Magnified OP phase image at the bottom edge of SPS crystal #1; (d) OP amplitude and phase versus bias voltage hysteresis loops in the crystal with a thickness of 143 μm; (e) Optical image and (f) corresponding OP image of SPS crystal #2; (g) Magnified OP phase, (h) amplitude and (i) topography images around the crack inside SPS crystal #2, the measured region was marked with a white box in Fig. 2(f).

monodomain.[28] However, the influence of electric field can be precluded, because the as-grown crystals were cooled down naturally in zero external electric field, as well as the strain gradient in bulk SPS crystals is negligible for providing a significant flexoelectric field. In addition, we carefully compared the elemental composition at the multi-domain and monodomain regions, as listed in Table 1. The almost identical elemental composition in two different regions excluded the role of defect. The formation of large-area monodomain is therefore attributed to a possible mechanism, that was, the screening of depolarization field, similarly to the monodomain in the thin ferroelectric oxide films realized by the screening effect of the extrinsic free charges.[24–26,29]

Since the SPS crystals were synthesized in the evacuated quartz tube, the screening charges may originate from the internal charge carriers of SPS crystal rather than from the external environment. It is noteworthy that the SPS crystal possesses a broad absorption band spanning the full-visible-light spectrum and a direct band gap of about 2.3 eV.[7] The illumination can induce the disproportionation reaction of Sn ions as in the following scheme:[30] $Sn^{2+} + h\nu = Sn^{3+} + e^-$; $2Sn^{3+} = Sn^{2+} + Sn^{4+}$. The conversion of the valence state of Sn ions can generate a large number of charge carriers, which are separated effectively by an internal electrical field.[31,32] The accumulation of positive and negative photoexcited charge carriers compensates the oppositely bound charges at both surfaces, leading to a screening of depolarization field,

Table 1. Elemental composition results in two different regions in SPS crystal.

Regions	Positions	Sn (%)	S (%)	P (%)
Multi-domain at the edges	P_1	21.67	58.66	19.67
	P_2	21.68	58.77	19.56
	P_3	21.60	58.67	19.74
	Mean	21.65 ± 0.04	58.70 ± 0.05	19.66 ± 0.07
Monodomain inside the crystal	P_4	21.75	58.65	19.60
	P_5	21.92	58.76	19.32
	P_6	21.82	58.39	19.79
	P_7	21.84	58.88	19.28
	Mean	21.83 ± 0.06	58.67 ± 0.18	19.50 ± 0.21

as illustrated in Fig. 3(a). In this case, the formation of ferroelectric domain wall to reduce the depolarization energy is nonessential,[33,34] or even not worthwhile, because the domain wall is energetically unfavored. The critical charge carrier concentration for monodomain in ferroelectrics can be roughly estimated with assumption that the surface-bound charges are fully compensated, i.e., $N'_{cr} = P_s/e = 1.1 \times 10^{13}$ cm^{-2} (where e is the elementary charge).

To characterize the charge carrier concentration in SPS crystals under the illumination, we performed current density-electrical field (J-E) measurements at room temperature, as shown in Fig. 3(b). The conductivity under the illumination was identified to be $\sigma = J/E = 1.14 \times 10^{-6}$ S/cm by fitting the linear ohmic region. The average charge carrier concentration was estimated with the correlation[35] of $N_{cr} = \sigma t/e\mu = 3.0 \times 10^{11}$ cm^{-2} (where $\mu = 2.4$ cm^2 V^{-1}s^{-1} is the reported charge carrier mobility[36] and t is the thickness of the sample), which was seven times larger than that measured in dark. The measured carrier concentration N_{cr} is lower than the estimated critical value N'_{cr}, due to the following possible reasons: (1) The value of estimated critical charge carrier concentration N'_{cr} is overestimated because fully screening at the surfaces is nonessential for the formation of monodomain. (2) The charge carrier concentration measured with current densityelectrical field (J-E) method is the volume average concentration. However, the charge carrier concentration at the surfaces is generally larger than that in bulk due to the fact that the charge carriers are separated by internal electrical field and accumulate at the surfaces. Therefore, the measured charge carrier concentration N_{cr} is underestimated. (3) The fact that the opaque silver electrodes weaken the light intensity and the contact resistance between the electrode and the
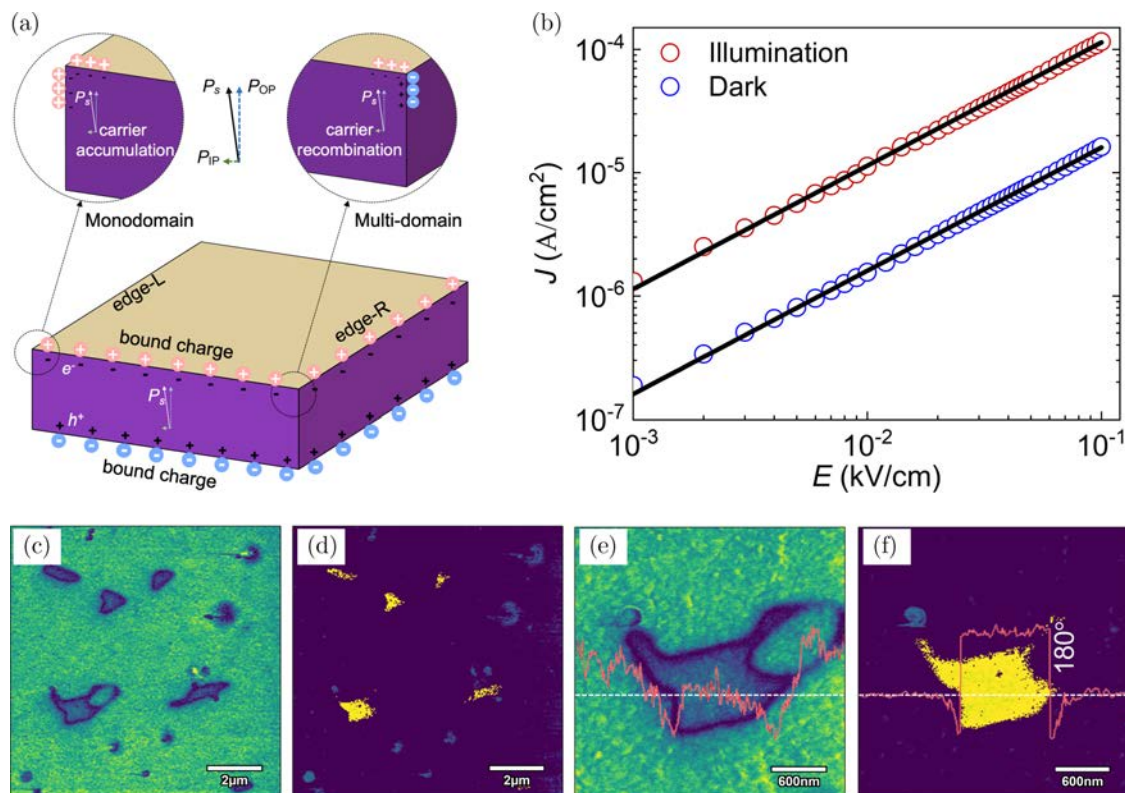

Fig. 3. (Color online) Photoexcited charge carriers analysis and ferroelectric domain distribution in SPS crystals annealed in dark. (a) Illustration of mechanism to describe the photoexcited charge carriers' screening effect and domain formations; (b) Current density-electrical field (J-E) curves of SPS crystals with a thickness of 1 mm; (c) OP amplitude and (d) phase images of annealed SPS crystal. The red line profile in (e) and (f) shows a weaker piezoresponse at domain wall and a 180° phase difference in two distinct regions, respectively.

sample also affects the measured conductivity, leading to a lower measured charge carrier concentration. To this end, we also calculated the upper charge carrier concentration from the conversion of the valence state of Sn ions measured from X-ray photoelectron spectroscopy (XPS) in previous work.[7] The XPS spectra results showed that ~7.8 % of Sn^{2+} ions were converted to Sn^{4+} ions under the illumination, generating a charge carrier concentration of 3.2×10^{13} cm^{-2}, which is larger than the estimated critical value N'_{cr}. Substantially, as the temperature increases to near the Curie temperature, the charge carrier concentration possesses an exponential enhancement, thus, is sufficiently larger than the critical value. Therefore, the final domain configuration is preferential monodomain.

In addition, given that the spontaneous polarization is not strictly perpendicular to the measured (011) surface, there is an in-plane polarization component.[7] According to the above mechanism of the screening effect with charge carriers, the in-plane polarization leads to the limited multi-domains at the edge of SPS crystal. As illustrated in the inset of Fig. 3(a), the in-plane polarization (labeled by green dashed arrow) perpendicularly points to the left side surface while the OP polarization (labeled by blue dashed arrow) vertically points to the top surface. The recombination and compensation probability of photoexcited charge carriers is much higher at the upper right edge (marked as "edge_R"), due to the oppositely bound charges at the top and right side surfaces. The recombination of charge carriers results in a strongly unscreened depolarization field at this edge, which drives the formation of a multi-domain. On the contrary, the same bound charges at the top and left side surfaces result in an accumulation of charge carriers at the upper left edge (marked as "edge_L"), which screens the depolarization field well. The expected different domains at two opposite edges is consistent with the experimental observation around the crack I in Fig. 2(f). Furthermore, since the propagation direction of crack II is perpendicular to that of crack I, the role of in-plane polarization component perpendicular to crack II is small, resulting in the same domain at two opposite sides of crack II. The special domain distributions at two opposite sides of the cracks I and II validate the above mechanism underlying the formation of monodomain again.

The above mechanism concludes that the photoexcited charge carriers are the key factor to the formation of the monodomain in SPS crystal. To further validate it, we performed an annealing experiment of SPS crystal in dark environment (wrapping the quartz tube with the aluminum foil) to rule out the influence of illumination as much as possible. The expected multi-domain was found in entire annealed SPS crystal, as shown in Figs. 3(c) and 3(d). The domains in yellow were scattered among the original domain in purple and its size was ~0.6 μm. The anti-parallel orientation of polarization in two different ferroelectric domains was also confirmed by the weaker piezoresponse at domain wall and the 180° phase difference in two distinct regions (Figs. 3(e) and 3(f)).

4. Conclusions

In summary, we obtained a large-area monodomain in as-grown bulk ferroelectric single crystals. A reproducible and stable monodomain is successfully achieved in bulk SPS crystals at room temperature. The underlying mechanism is attributed to the limited depolarization field, which is screened by the photoexcited charge carriers from the disproportionation reaction of Sn ions. Our work offers a potential approach for designing bulk ferroelectrics with monodomain which is desirable for improving the electro-optic devices performances.

References

[1] J. Shi, X. Liu and W. Tian, High energy-storage properties of $Bi_{0.5}Na_{0.5}TiO_3$-$BaTiO_3$-$SrTi_{0.875}Nb_{0.1}O_3$ lead-free relaxor ferroelectrics, *J. Mater. Sci. Technol.* **34**, 2371 (2018).

[2] Z. Wen, C. Li, D. Wu, A. Li and N. Ming, Ferroelectric-field-effect-enhanced electroresistance in metal/ferroelectric/semiconductor tunnel junctions, *Nat. Mater.* **12**, 617 (2013).

[3] J. Wang *et al.*, Logic and in-memory computing achieved in a single ferroelectric semiconductor transistor, *Sci. Bull.* **66**, 2288 (2021).

[4] T. Xu, P. Niu, S. Wang and L. Li, High visible light photocatalytic activities obtained by integrating g-C_3N_4 with ferroelectric $PbTiO_3$, *J. Mater. Sci. Technol.* **74**, 128 (2021).

[5] S. Huang *et al.*, Flexoelectricity in dielectrics: Materials, structures and characterizations, *J. Adv. Dielect.* **8**, 1830002 (2018).

[6] R. V. Gamernyk, Y. P. Gnatenko, P. M. Bukivskij, P. A. Skubenko and V. Y. Slivka, Optical and photoelectric spectroscopy of photorefractive $Sn_2P_2S_6$ crystals, *J. Phys. Condens. Matter.* **18**, 5323 (2006).

[7] J. Deng *et al.*, Enhanced domain wall conductivity in photosensitive ferroelectrics $Sn_2P_2S_6$ with full visible spectrum absorption, *Sci. China Mater.* **65**, 1049 (2021).

[8] D. Haertle *et al.*, Electro-optical properties of $Sn_2P_2S_6$, *Opt. Commun.* **215**, 333 (2003).

[9] R. Ryf *et al.*, High-frame-rate joint Fourier-transform correlator based on $Sn_2P_2S_6$ crystal, *Opt. Lett.* **26**, 1666 (2001).

[10] F. Juvalta, R. Mosimann, M. Jazbinšek and P. Günter, Fast dynamic waveguides and waveguide arrays in photorefractive $Sn_2P_2S_6$ crystal induced by visible light, *Opt. Exp.* **17**, 379 (2009).

[11] G. Catalan, J. Seidel, R. Ramesh and J. F. Scott, Domain wall nanoelectronics, *Rev. Mod. Phys.* **84**, 119 (2012).

[12] G. F. Nataf *et al.*, Domain-wall engineering and topological defects in ferroelectric and ferroelastic materials, *Nat. Rev. Phys.* **2**, 634 (2020).

[13]M. Fiebig, T. Lottermoser, D. Meier and M. Trassin, The evolution of multiferroics, *Nat. Rev. Mater.* **1**, 16046 (2016).

[14]K. Buse, A. Adibi and D. Psaltis, Non-volatile holographic storage in doubly doped lithium niobate crystals, *Nature* **393**, 665 (1998).

[15]D. Sando *et al.*, Epitaxial ferroelectric oxide thin films for optical applications, *Appl. Phys. Rev.* **5**, 041108 (2018).

[16]L. Landau and E. Lifshitz, *Perspectives in Theoretical Physics* (Pergamon, Oxford, 1992).

[17]C. Kittel, Theory of the structure of ferromagnetic domains in films and small particles, *Phys. Rev.* **70**, 965 (1946).

[18]T. Mitsui and J. Furuichi, Domain structure of rochelle salt and KH_2PO_4, *Phys. Rev.* **90**, 193 (1953).

[19]A. Schilling *et al.*, Scaling of domain periodicity with thickness measured in $BaTiO_3$ single crystal lamellae and comparison with other ferroics, *Phys. Rev. B* **74**, 024115 (2006).

[20]S. K. Streiffer *et al.*, Observation of nanoscale 180° stripe domains in ferroelectric $PbTiO_3$ thin films, *Phys. Rev. Lett.* **89**, 067601 (2002).

[21]M. Hehn, S. Padovani, K. Ounadjela, and J. P. Bucher, Nanoscale magnetic domain structures in epitaxial cobalt films, *Phys. Rev. B* **54**, 3428 (1996).

[22]O. Nesterov *et al.*, Thickness scaling of ferroelastic domains in $PbTiO_3$ films on $DyScO_3$, *Appl. Phys. Lett.* **103**, 142901 (2013).

[23]L. Chen *et al.*, Thickness dependence of domain size in 2D ferroelectric $CuInP_2S_6$ nanoflakes, *AIP Adv.* **9**, 115211 (2019).

[24]G. Liu *et al.*, Positive effect of an internal depolarization field in ultrathin epitaxial ferroelectric films, *Adv. Electron. Mater.* **2**, 1500288 (2016).

[25]D. D. Fong *et al.*, Stabilization of monodomain polarization in ultrathin $PbTiO_3$ films, *Phys. Rev. Lett.* **96**, 127601 (2006).

[26]C. Lichtensteiger, S. Fernandez-Pena, C. Weymann, P. Zubko and J.-M. Triscone, Tuning of the depolarization field and nanodomain structure in ferroelectric thin films. *Nano Lett.* **14**, 4205 (2014).

[27]S. Matzen *et al.*, Super switching and control of in-plane ferroelectric nanodomains in strained thin films, *Nat. Commun.* **5**, 4415 (2014).

[28]D. Lee *et al.*, Giant flexoelectric effect in ferroelectric epitaxial thin films, *Phys. Rev. Lett.* **107**, 057602 (2011).

[29]R. Takahashi, Ø. Dahl, E. Eberg, J. K. Grepstad and T. Tybell, Ferroelectric stripe domains in $PbTiO_3$ thin films: Depolarization field and domain randomness, *J. Appl. Phys.* **104**, 064109 (2008).

[30]A. A. Grabar, Light-induced electric conductivity in $Sn_2P_2S_6$, *Ferroelectrics* **192**, 155 (1997).

[31]S. Y. Yang *et al.*, Above-bandgap voltages from ferroelectric photovoltaic devices, *Nat. Nanotechnol.* **5**, 143 (2010).

[32]Y. Liu *et al.*, Internal-field-enhanced charge separation in a single-domain ferroelectric $PbTiO_3$ photocatalyst, *Adv. Mater.* **32**, 1906513 (2020).

[33]A. Kopal, T. Bahnik and J. Fousek, Domain formation in thin ferroelectric films: The role of depolarization energy, *Ferroelectrics* **202**, 267 (1997).

[34]J. F. Scott, Nanoferroelectrics: Statics and dynamics, *J. Phys. Condens. Mat.* **18**, R361 (2006).

[35]D. Shi *et al.*, Low trap-state density and long carrier diffusion in organolead trihalide perovskite single crystals, *Science* **347**, 519 (2015).

[36]A. Regmi, I. Biaggio and A. A. Grabar, Optical determination of the charge carrier mobility in $Sn_2P_2S_6$, *Appl. Phys. Lett.* **109**, 182104 (2016).